Steel and Composite Structures, *Vol. 26, No. 6 (2018) 719-731*
DOI: https://doi.org/10.12989/scs.2018.26.6.719

Experimental study on the seismic performance of concrete filled steel tubular laced columns

Zhi Huang [1,2a], Li-Zhong Jiang [*1], Y. Frank Chen [**3,4], Yao Luo [1b] and Wang-Bao Zhou [1c]

[1] *School of Civil Engineering, Central South University, Changsha 410075, China*
[2] *School of Civil Engineering, Hunan University of Science and Technology, Xiangtan 411201, China*
[3] *School of Engineering and Technology, Southwest University, Chongqing 400716, China*
[4] *Department of Civil Engineering, The Pennsylvania State University, Middletown 17057, PA, USA*

(*Received April 16, 2017, Revised December 2, 2017, Accepted January 16, 2018*)

Abstract. Concrete filled steel tubular (CFST) laced columns have been widely used in high rise buildings in China. Compared to solid-web columns, this type of columns has a larger cross-section with less weight. In this paper, four concrete filled steel tubular laced columns consisting of 4 main steel-concrete tubes were tested under cyclic loading. Hysteresis and failure mechanisms were studied based on the results from the lateral cyclic loading tests. The influence of each design parameter on restoring forces was investigated, including axial compression ratio, slenderness ratio, and the size of lacing tubes. The test results show that all specimens fail in compression-bending-shear and/or compression-bending mode. Overall, the hysteresis curves appear in a full bow shape, indicating that the laced columns have a good seismic performance. The bearing capacity of the columns decreases with the increasing slenderness ratio, while increases with an increasing axial compression ratio. For the columns with a smaller axial compression ratio (< 0.3), their ductility is increased. Furthermore, with the increasing slenderness ratio, the yield displacement increases, the bending failure characteristic is more obvious, and the hysteretic loops become stouter. The results obtained from the numerical analyses were compared with the experimental results. It was found that the numerical analysis results agree well with the experimental results.

Keywords: concrete filled steel tubular laced columns; seismic performance; low cyclic loading; restoring force model; hysteresis curve

1. Introduction

Concrete filled steel tubular (CFST) laced columns are a structure composed of two or more column limbs which are connected by transverse lacing bars. Each CFST laced column consists of 2-4 tubes (Fig.1) with 4 tubes being most common in China. This study aims to investigate the seismic performance of four-tube CFST laced columns. The column limbs are composed of concrete filled steel tubes primarily for withstanding compressive forces. Despite of smaller column diameter, this built-up section has greater stiffness as it consists of multiple column limbs. Therefore, this type of structural assembly is more advantageous in the situations of large load eccentricity and/or high slenderness ratio (Patel *et al*. 2017). CFST laced columns have been widely used in large-span structures and bridges (Yang *et al*. 2015). For examples, in recent years in China, four-tube CFST laced columns were used in places like Tianjin Taida International Convention and Exhibition Center, Wuxia Yangtze River Bridge in Sichuan province, and Dongguan Shuidao super large bridge in Guangdong Province (Han and Yao 2004). Research on the seismic performance of four-tube CFST laced columns has not been conducted sufficiently. The limited number of investigation reports focus on the axial compressive and flexural behavior rather than the lateral hysteretic behavior of CFST laced columns (e.g. Lachemi *et al*. 2006 and Xiao *et al*. 2017). Consequently, more detailed investigation of the seismic behavior of four-tube CFST laced columns is necessary.

Experimental and theoretical studies on the seismic performance of CFST laced columns have been performed by a number of researchers. For examples, Hassanein *et al*. (2015) investigated the axial compressive performance of CFST laced columns with inner circular tubes. A new design model was proposed to predict the ultimate axial strength of short CFST columns compared with the Eurocode 4. Kawano and Sakino (2003) presented the experimental results of a series of studies on CFST laced columns and proposed a better seismic resistance structural system by introducing some CFST laced columns into the corresponding steel frames. Their test results showed that CFST laced columns could limit the structural bending deformation similarly to the shear wall in a reinforced concrete structure (Akihiko and Chiaki 2002 and Kawano and Sakino 2003). Based on the results from the extensive experiments using low cyclic loading, an improved

*Corresponding author, Professor,
E-mail: lzhjiang@csu.edu.cn
** Corresponding author, Professor,
E-mail: yxc2@psu.edu
[a] Ph.D., E-mail: huangzhi@csu.edu.cn
[b] P.E., E-mail: 280915377@qq.com
[c] Associate Professor, E-mail: zhouwangbao@163.com

ISSN: 1229-9367 (Print), 1598-6233 (Online)

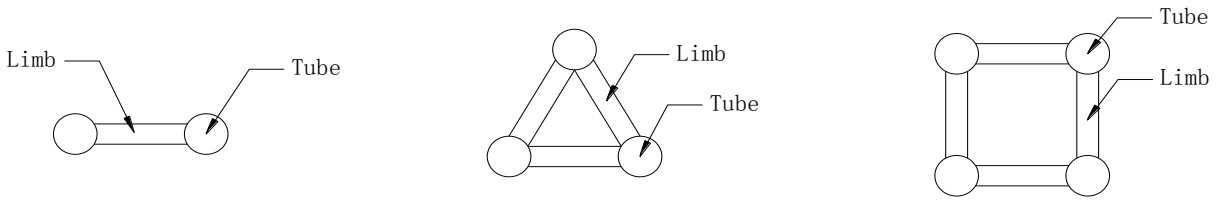

(a) Two-tube CFST columns (b) Three-tube CFST columns (c) Four-tube CFST columns

Fig. 1 Types of CFST laced columns

numerical method to predict the elastic and plastic ultimate bearing capacities of CFST lattice columns has been proposed (Jiang *et al*. 2010). Ou *et al*. (2011) carried out a series of experiments on CFST laced columns to quantify the column failure mechanism at ultimate loads. These simplified methods have been continually improved to analyze static/seismic performance of members. However, a validation and extensive seismic performance are required before they can be reliably used and addressed in codes.

Studies on CFST laced columns of single tube have been extensively done, including circular, square, and rectangular shapes. Kalochairetis and Gantes (2011) investigated the collapse load of built-up columns and compared their analysis method with EC3 specifications. Portolés *et al*. (2011) performed experiments on 37 specimens of slender circular concrete-filled composite columns subjected to eccentric axial loads and established the advisability of use of high strength concretes for CFST columns by comparing their performance indices with normal strength concretes. The typical failure mode for all 37 specimens was the overall buckling mode rather than the material failure; it is shown that the use of high strength concrete on CFST laced columns is advisable. Based on these studies, Portolés *et al*. (2013) extended the study on ultra-high strength infill in slender CFST columns and established a good option for practical applications. Since then, improvement on the compression models has been progressively made to obtain the ultimate strength, ductility, and collapse behavior of concrete-filled composite columns. Choi *et al*. (2014) carried out an experimental investigation on structural performance of mega column to spandrel beam connections used in high-rise building by using two specimens with 1/5 scale. While performing extensive small-scale experiments, the computer program to perform the numerical analysis for composite columns under axial compressive load and single curvature bending was performed (Abed *et al*. 2013). Jayaganesh *et al*. (2015) investigated the behavior of circular and square CFST stub columns under local compression based on a combined experimental and numerical study. The aforementioned studies mostly concentrate on the study of single tube CFST laced column and the improved compression models through these studies can be used for four-tube columns, whereas the research for the lateral cyclic loading tests does exist but of limited. Next, the researchers had not reported how the limbs affect the horizontal performance of CFST laced columns.

Furthermore, studies on CFST laced columns have largely been left out, especially for the seismic performance under lateral cyclic loading. A comprehensive study has been conducted to investigate the behavior and strength of these members under static loading, such as the ultimate load capacity under axial compression (Jiang *et al*. 2010) or eccentric compression (Li *et al*. 2016). Previous studies focused on static rather than seismic performance. Researches related to the seismic performance of CFST laced columns especially hysteretic behavior are relatively limited. Related studies on the seismic behavior of CFST laced columns considered the parameter of the ratio of steel to concrete strengths, eccentricity ratio, slenderness ratio, or steel ratio only. In this study, to fully understand the seismic performance of CFST laced columns, the influence of the system parameters on skeleton curves, hysteretic behavior, load-strain relationship, displacement ductility, and stiffness degradation were investigated. The considered parameters include equivalent slenderness ratio λ_x^*, axial compression ratio *n*, and tube thickness *t*. Due to the complexity of the CFST laced column section and the tedious calculation involved, the equivalent slenderness ratio λ_x^* is usually used by the engineering community in China, as expressed in Eq. (1)

$$\lambda_x^* = \sqrt{\lambda_x^2 + 40\frac{A_0}{A_{1x}}} \tag{1}$$

with

$$\lambda_x = \frac{l_e^*}{\sqrt{\frac{I_x}{A_0}}} \tag{2}$$

where l_e^* is the equivalent length of a CFST laced column, I_x is the moment of inertia with respect to *x* axis, A_0 is the sum of sectional areas of all limbs, and A_{1x} is the sum of the gross sectional areas of all diagonal lacing tubes perpendicular to *x* axis.

2. Experiment procedure

2.1 Geometric properties of specimens and considered variables

A total of 4 CFST laced column specimens were tested under low cyclic loading. The properties for the specimens are indicated in Table 1 along with the three main system parameters affecting the seismic performance of CFST laced columns (i.e., axial compression ratio, equivalent slenderness ratio, and tube thickness). In order to reduce the

Table 1 Properties of test specimens

Specimen number	Length /mm	Tube thickness /mm	Axial compression ratio	Equivalent slenderness ratio	Axial bearing capacity /kN	Axial loading /kN
SCC1	1200	2.5	0.2	10.8	1184	236.8
SCC4	1200	2.5	0.3	10.8	1184	355.2
SCC5	2100	2.5	0.2	18.4	1160	232
SCC6	3000	2.5	0.2	27.9	1043	208.6

Table 2 Main construction variables of test specimens

External diameter of limbs	86 mm	Node distance	300 mm
Thickness of limbs	1.5 mm	External diameter of tube	48 mm
Spacing between limbs	300 mm	Confinement coefficient	0.82

total cost of experiments and improve the test efficiency, the orthogonal array method as proposed by Hedayat *et al.* (1999) was adopted in this study, which ensures the uniformity of the distribution of the system parameters and their variations during the experiments. All 4 specimens were prepared with the same section size of 386 mm × 386 mm. In this study, the size of limbs, the node distance and the limb spacing were kept the same, where the external diameter = 86 mm, thickness = 1.5 mm, and node distance = 300 mm (Table 2). The limb was cut from a seamless steel tube with the yield strength of 235 MPa and filled with concrete of 20.41 MPa strength, where the tube thickness varies from 2 mm to 3 mm (Table 1) and tube outer diameter = 48 mm typically (Table 2).

To ensure that the column ends are restrained as intended, the base and prop cap of a CFST laced column were cast with the concrete adequately reinforced with 16 mm Φ longitudinal bars (HRB335) and 8 mm φ stirrups (HPB235). To assure the base to function as intended prior

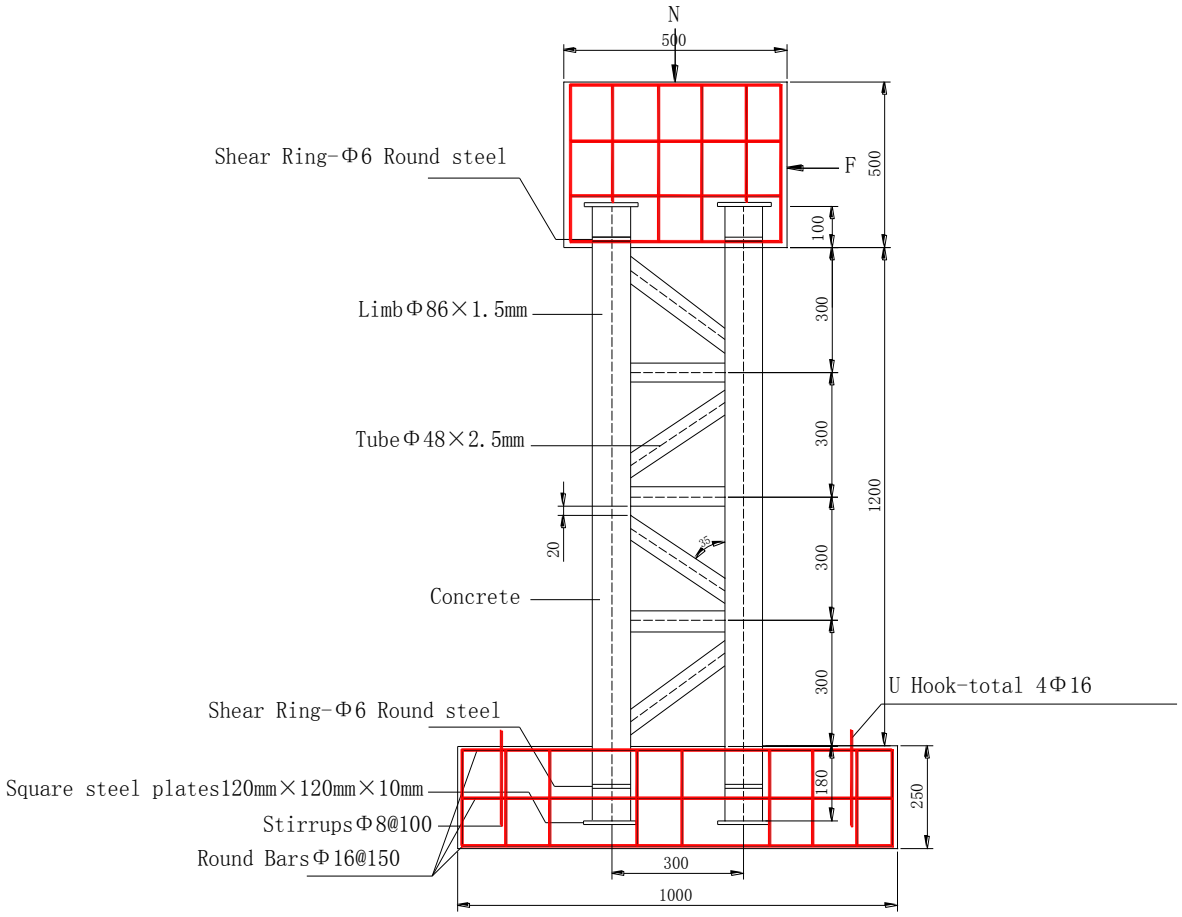

*Notes: All units in mm; φ and Φ = bar diameters represent stirrups of HPB 235 plain steel bar and HRB 335 hot rolling ribbed reinforcing bar, respectively

Fig. 2 Geometry and instrumentation of test specimens

to a specimen's failure, each CFST laced column was fixed on a rigid reinforced concrete foundation of 250 mm (height) × 600 mm (width) × 1000 mm (length) which was reinforced with the same size of reinforcing steel (Fig. 2). The prop cap at the top of each specimen was formed with 500 mm × 500 mm × 500 mm cubic reinforced concrete (Fig. 2). The column was extended by 100 mm at the top and 180 mm at the bottom, making its total length 280 mm longer (Fig. 2).

2.2 Material mechanical properties and specimen preparation

According to China's test specifications and standards GB50010 (2010a), the design concrete compressive strength f_{cu} of 150 mm × 150 mm × 150 mm cubic samples and the concrete elastic modulus E_c of 100 mm × 100 mm × 300 mm samples must be obtained. Through the measured f_{cu} values, the axial compressive strength f_c and the axial tensile strength f_t of concrete can be obtained from Eqs. (3) and (4) respectively, which are described in Guo (1999). The elastic modulus of concrete may be determined by the empirical formula Eq. (5) as adopted in the design code GB50010 (2010b). As a result, the average mechanical properties of concrete are listed in Table 3, in which the specimens were cast at the same time and maintained under the same condition.

$$f_c = 0.76 f_{cu} \tag{3}$$

Table 3 Average mechanical properties of concrete

f_{cu} (MPa)	f_c (MPa)	f_t (MPa)	E_c (MPa)
20.41	15.51	1.94	25640

$$f_t = 0.26 f_{cu}^{2/3} \tag{4}$$

$$E_c = \frac{10^5}{2.2 + \frac{34.7}{f_{cu}}} \tag{5}$$

The average yield strength of steel limbs f_y = 315 MPa, ultimate strength of steel limbs f_u = 390 MPa, yield strength of steel tubes f_y = 320 MPa, ultimate strength of steel tubes f_u = 400 MPa, and elastic modulus of steel (limbs and tubes) E_s = 2.06×10^5 MPa, which were obtained based on the tensile strength test results reported by Gong *et al*. (2010).

120 mm × 120 mm × 10 mm steel plate was used at both ends of each specimen, with its geometric center coinciding with that of the limb. The diagonal tubes are arranged as "K" shape and the angle between the diagonal and vertical tubes is 35 degrees. A gap of 20 mm between the horizontal and diagonal tubes was kept to avoid the concentrated stress. The vertical spacing between two adjacent horizontal tubes is 300 mm (Fig. 3).

2.3 Test setup and loading history

The test setup is shown in Fig. 3, where the lower end of the specimen was assumed to be fixed and the top end free. The MTS system generates the lateral loading with 1000 kN through its horizontal servo actuator and includes 980 kN manual hydraulic jack to produce the initial constant vertical axial loading. To ensure that the jack produces only the vertical axial loading as intended, a special steel loading plate was placed under the jack. This also avoids the local failure of the concrete cap.

The test used a pseudo-static test program. Under an axial compression ratio, the low cyclic displacement was

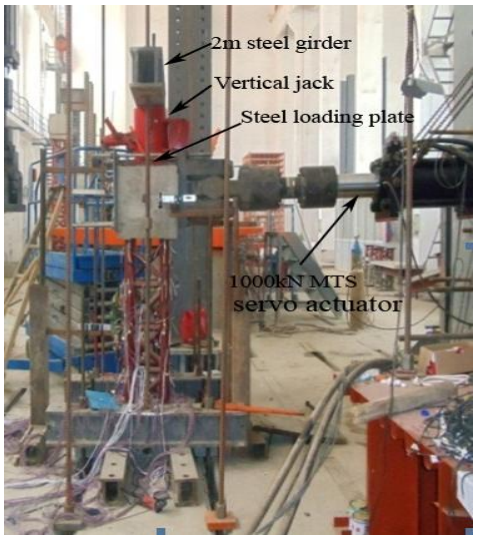

(a) Overview

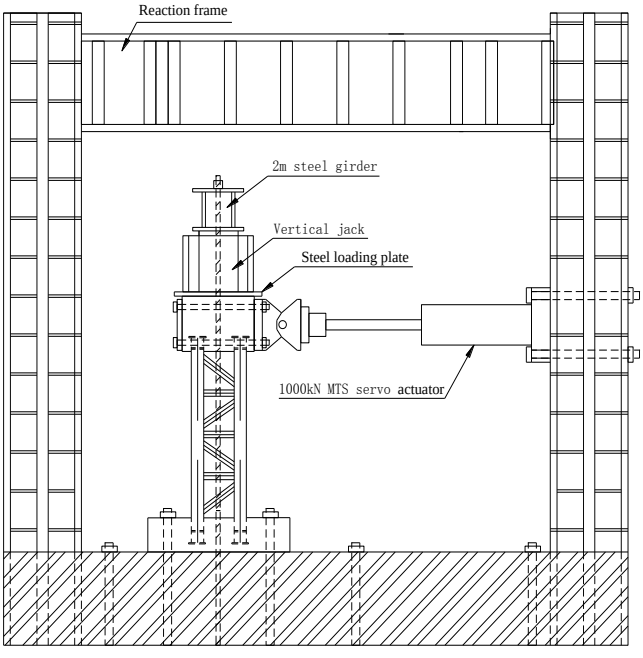

(b) Schematic layout

Fig. 3 Test setup

applied to the CFST laced column. Each test involved the following three steps:

(1) Application of axial compression
The CFST laced column was preloaded to 40-60% of the intended test axial load to make sure the working in each part of the specimen. This step also assured that all apparatus and instruments were working and reliable. After the alignment, the load was kept constant to the axial compressive force of the CFST laced columns and the test started. Pressure was continuously applied for 2-3 minutes.

(2) Application of horizontal cyclic displacement
The specimen was then gradually loaded with a horizontal cyclic displacement. Specifically, the specimen was initially loaded with 50% of the calculated yield displacement and the remaining 50% was loaded until the specimen yielded. After that, each loading increment was set to be equal to the calculated yield displacement.

(3) Termination of loading
When any of the following situations occurs, the specimen is considered to reach the failure condition and the loading or test should be terminated.
(a) The first cyclic displacement is less than 85% of the maximum loads.
(b) The loading displacement exceeds 1/200 of the specimen height.
(c) A drum deformation is detected at the column bottom with obvious tearing or other failure phenomenon.

3. Test results

3.1 Observations and failure modes

Specimens SCC1 and SCC4 having a lesser shear-span ratio display a compression bending shear failure. Both specimens experience a similar failure process. At the beginning of the loading, the stress and deformation of the specimens show a steady development and the displacement increases proportionally with the increasing load. When the displacement reaches 32 mm (about 4 times of the yield displacement), the bottom of the CFST laced column begins to show a drum deformation (Fig. 4) on the compression side, but no local deformation was observed for the two limbs on the other side of the column. As shown in Fig. 4, the paint coating surface on the CFST laced columns was peeled off due to the squeezing of the steel pipe by the enclosed concrete. This indicates that there is a certain slip between the steel pipe and the concrete. However, by reversing the loading at this stage, the drum deformation would be completely recovered, which suggests that the bearing capacity of the specimens is not affected prior to the appearance of the torn cracks on the limbs and the ductility of the CFST laced column is fairly good. Increasing the load to reach a displacement of 48 mm, the drum displacement cannot be recovered anymore and gradually spreads outward and radially. When the displacement reaches 60 mm, the drum displacement becomes very apparent and the horizontal cracks appear on the compression side accompanied with a few spalled concrete fragments. This indicates that the bottom concrete in the specimen has been crushed. Increasing the load further to

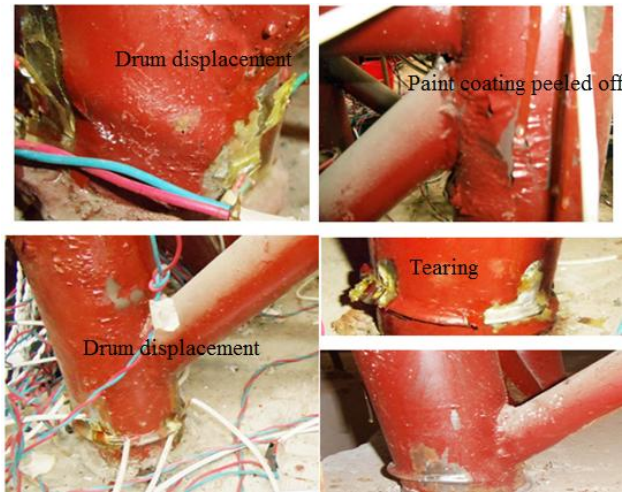

Fig. 4 Typical failure modes of specimens

Fig. 5 Total failure of specimens

72 mm displacement level, the bearing capacity of the column decreases obviously and the tearing on both sides of limbs at the column bottom was observed (Fig. 4), indicating that the specimen has been destroyed. At this stage, the total in-plane bending deformation becomes more extensive.

For Specimen SCC5, which has a larger shear span, the initial local buckling of limbs at the column bottom appears when the load reaches the displacement level of 48 mm (about 3 times of the yield displacement). At this stage, the local buckling of limbs would be recovered if the loading is terminated. Increasing the load to the displacement level of 72 mm, the drum displacement cannot be recovered and visible drum displacement was observed (Fig. 4). By increasing the load to 84 mm displacement level, the bearing capacity starts to decrease and the limbs begin to experience the drum displacement until the members are torn-out. Compression bending failure plus a horizontal crack near the column bottom was observed. The failure of Specimen SCC5 is shown in Fig. 5.

Specimen SCC6 as a long column experiences an obviously total deformation during the entire loading process and shows a compression bending failure. When the displacement reaches 90 mm, slight local deformation appears which can be fully recovered if unloaded. With the horizontal displacement increased to 120 mm, the local deformation of the specimen can no longer be completely recovered. Increasing the load to 150 mm displacement level, in-plane bending obviously appears and the drum deformation at the column bottom shows up, but unlike other specimens no horizontal crack was observed. At this point, the loading or test has to be terminated due to the limit of MTS actuator.

3.2 Hysteretic behavior

The hysteretic curve for each CFST laced column is used as the basis to evaluate the dissipated energy and can approximately reflect the seismic performance of specimens. It is also the basis for determining the non-linear restoring force and seismic response. In general, there are four shapes for the hysteretic curve: (a) Spindle-shape; (b) Bow-shape; (c) Reverse S-shape; and (d) Z-shape. A wider hysteretic loop means better seismic performance or greater energy dissipation capacity.

In this study, a displacement meter was arranged at the position of MTS loading during the test. The sensor installed inside the MTS actuator records the top horizontal forces. As a result, the horizontal force-displacement relationships at the top of the specimens are shown in Fig. 7.

For Specimens SCC1 and SCC4 with different axial compression ratios, the hysteretic curves appear as a bow-shape. Overall, the hysteretic loops are somewhat larger but smaller than the spindle shape with an insignificant pinch phenomenon because of the slip and shear deformation developed. During the elastic range, the deformation is nearly 100 percent recovered after unloading and the area enclosed by the hysteretic loops representing the energy dissipation is negligible. The CFST laced columns seem to have a greater plastic deformation capacity and can thus absorb more energy during an earthquake.

For Specimen SCC5, the hysteretic curve appears as a reverse S-shape instead. The hysteretic curve is not stout because there is a significant slip between the steel and the concrete, especially during the later loading stage as observed from the more apparent pinch phenomenon. The pouring quality of the concrete in a long column is more difficult to be achieved and thus attributes to such slips. Note also that the shear deformation, which cannot be ignored, weakens the energy dissipation capacity of a specimen with less shear span ratio. This combined effect results in a less fattened hysteretic curve.

For Specimen SCC6, the hysteretic curve is the stoutest one, close to the spindle shape. Because the shear span ratio of this specimen is larger than the others, its bending

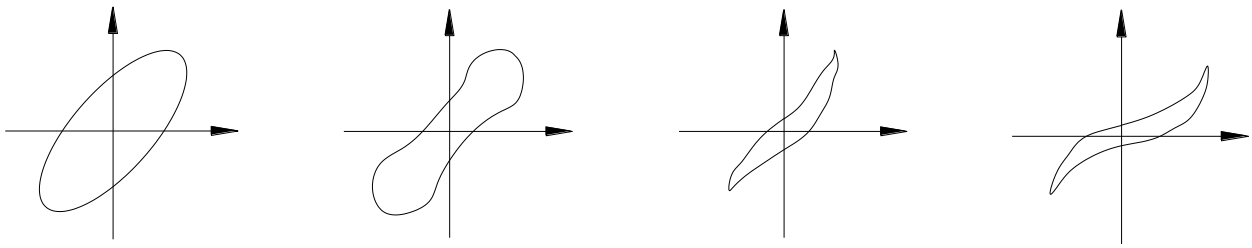

(a) Spindle-shape (b) Bow-shape (c) Reverse S-shape (D) Z-shape

Fig. 6 Hysteretic curve shapes

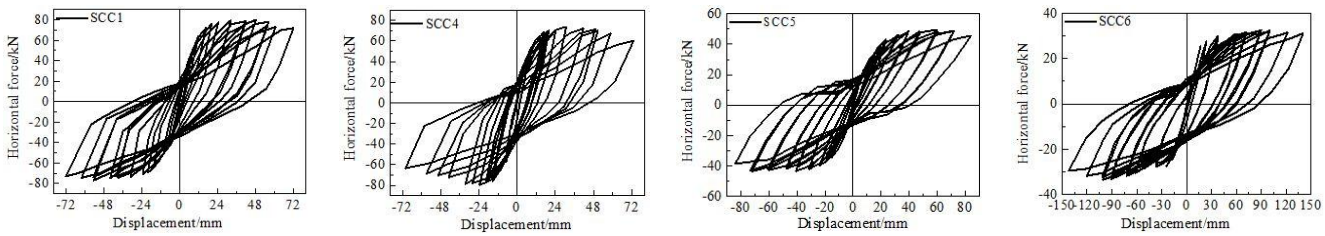

Fig. 7 Horizontal force-displacement hysteretic curves at the top of the specimens

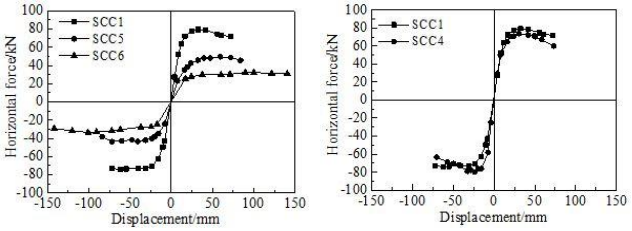

Fig. 8 Horizontal force-displacement skeleton curves at the top of the specimens

performance could be significantly developed under horizontal forces and hence results in a perfect hysteretic curve. In contrast, the shear deformation in Specimen SCC6 is negligible. The small contraction occurring during the later loading stage is primarily due to the slip between the steel and the concrete. So, the slenderness ratio has a larger effect on the shape of the hysteretic curves for CFST laced columns.

3.3 *Skeleton curve*

The skeleton curve is commonly defined as the envelope of a force-displacement curve, i.e., the path of the successive peaks of the first cycle at each load level. It is usually used to characterize the hysteretic behavior and ductility capacity of steel and steel-concrete composite members subjected to load reversals. The skeleton curves of the test specimens are shown in Fig. 8.

As seen, the skeleton curves consist of three stages: elastic, elastic-plastic, and failure. The initial stiffness for Specimens SCC1, SCC5, and SCC6, which have smaller slenderness ratios, is higher. Although the peak force values are different, the shapes of the skeleton curves are similar.

The lager the slenderness ratio of CFST laced columns is, the smaller the stiffness during the elastic stage, as evidenced from the lower horizontal bearing capacity. However, for Specimens SCC1 and SCC4, their initial stiffness is nearly equal for different axial compression ratios as they have the same equivalent slenderness ratio $\lambda_x^* = 10.8$. The stiffness during the failure stage would become slightly larger for the specimens with a larger axial compression ratio, compared to the other two stages. Hence, the effect of axial compression ratio on the seismic behavior appears to be more significant during the failure stage.

3.4 *Loading-strain curve*

Fig. 9 shows the load versus strain curves, based on the measured data collected at four selective locations along the height of each specimen. The longitudinal strains of limbs tend to increase along the height. The loading-longitudinal strain hysteretic curve at the member's bottom looks as a

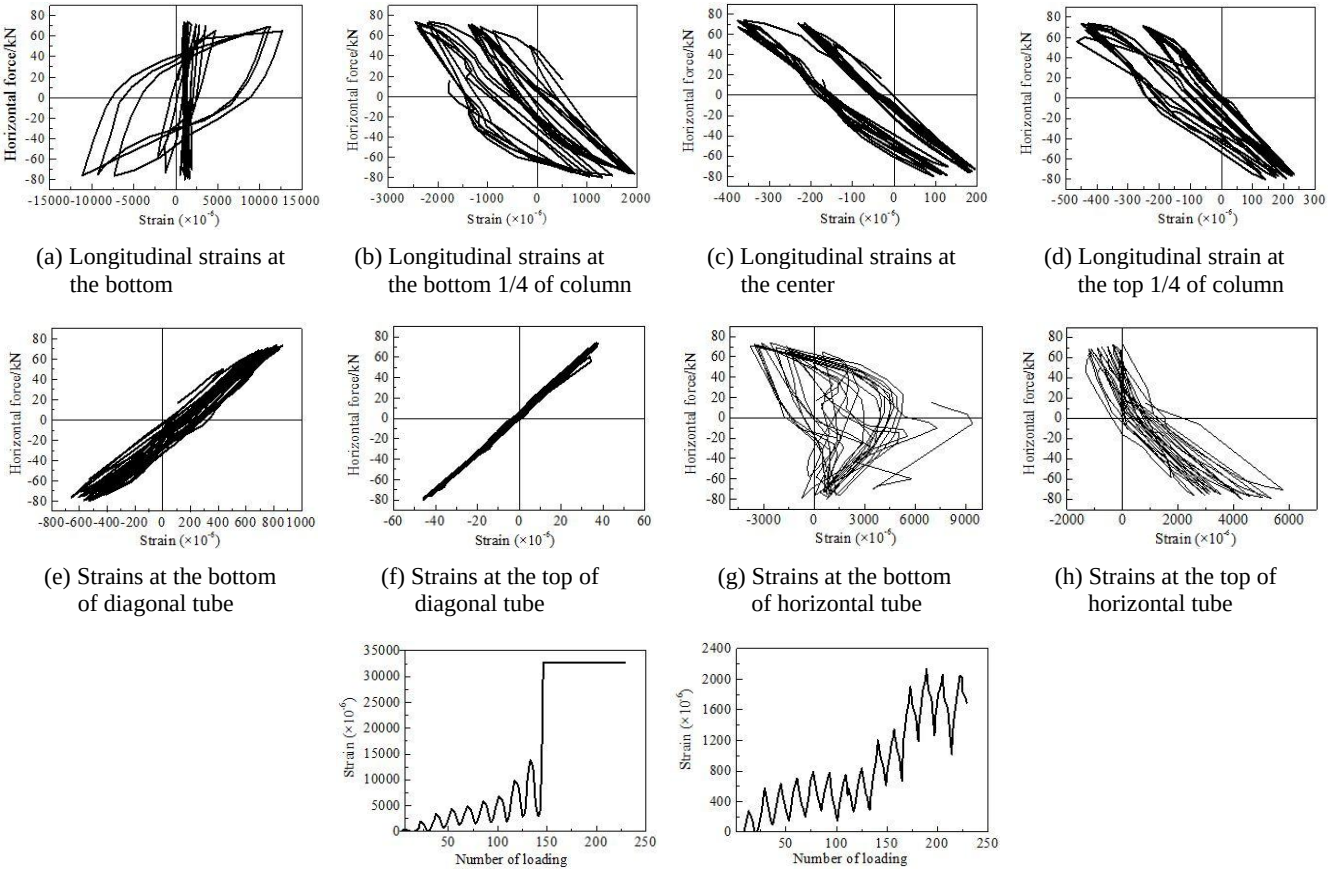

(a) Longitudinal strains at the bottom

(b) Longitudinal strains at the bottom 1/4 of column

(c) Longitudinal strains at the center

(d) Longitudinal strain at the top 1/4 of column

(e) Strains at the bottom of diagonal tube

(f) Strains at the top of diagonal tube

(g) Strains at the bottom of horizontal tube

(h) Strains at the top of horizontal tube

(i) Hoop strains at the bottom

(j) Hoop strains at the bottom 1/4 of column

Fig. 9 Load versus strain curves of test specimens

plump spindle-shape (Fig. 9(a)), indicating that the steel tube in this area has yielded. However, the longitudinal strains along the height (Figs. 9(b)-(d)) are still in the elastic stage, implying that the corresponding stresses of each specimen do not vary much.

For the secondary diagonal tubes (Figs. 9(e)-(h)), their longitudinal strains display a linear variation under the cycling loading. The strains of the horizontal tubes do not show a significant variation, however.

As shown in Figs. 9(i) and (j), the hoop strains in the limbs are all tensile and increase with the loading until the ultimate load is reached. The hoop strain at the bottom of the test specimens could be recovered in the early stage according to the loading cycles, whereas at a later time it could not be recovered due to the increasing deformation. At this time, the steel hoop yields and the strain gauge fails. The hoop strains in the quarter of CFST laced columns show an increasing trend but remain elastic prior to the failure. This suggests that the failure of CFST laced columns initiates at the bottom. Moreover, the confinement effect between the steel and the concrete is more obvious at the bottom of the test columns.

3.5 Deformation restoring capacity

The deformation restoring capacity is generally good as the structural deformation can be almost recovered after an earthquake, thereby facilitating the post-earthquake repair work. The deformation restoring ratio, γ_i, is defined by Eq. (6)

$$\gamma_i = \Delta_r^i / \Delta_{max}^i \tag{6}$$

where Δ_r^i is the maximum displacement of the i-th cycle and $\Delta_{\max}^i$ is the residual displacement of the i-th cycle.

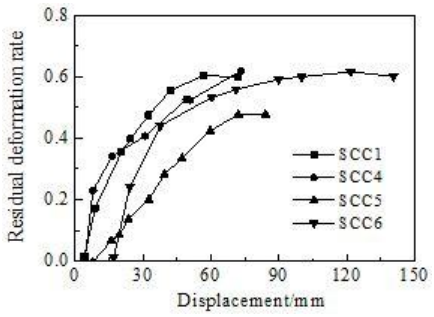

Fig. 10 Residual deformation rate curves of test specimens

Fig. 10 shows the residual deformation rate curves of test specimens. The residual deformation rate becomes larger with the increased loading. During the early loading stage, the variation of residual displacements is nearly linear. The increasing rate becomes slower at a later loading stage. The average residual displacement ratio is greater than 0.5, indicating that the test specimens have a good.

3.6 Displacement ductility

The definition of displacement ductility is available in the literature. After determining the skeleton curve and maximum horizontal force $P_{\max}$, the yield and ultimate displacements can be defined by connecting the origin of the skeleton curve with the point corresponding to the force value of $0.75P_{\max}$ on the curve and then extending the line to intersect with the horizontal line corresponding to the peak loading (Fig. 11). The abscissa of the intersection point B is the yield displacement Δ_y. The displacement corresponding to the force of $0.85P_{\max}$ is the ultimate displacement Δ_u. The displacement ductility μ is thus defined by

$$\mu = \Delta_u / \Delta_y \tag{7}$$

The obtained μ values are summarized in Table 4, which range approximately between 3 and 4, implying the CFST laced columns have fairly good displacement ductility according to the Chinese design code GB50011-2010. Specimens SCC1, SCC5, and SCC6, which have a lower axial compression ratio at 0.2, have a better ductility (μ = 4.04) than Specimen SCC4 (μ = 3.62). The higher the ductility ratio is, the better the seismic performance. Consequently, the axial compression ratio is a key factor influencing the displacement ductility of CFST laced columns. Furthermore, the axial compression ratio affects the deformation and failure modes of CFST laced columns and the bearing capacity during the entire test process. With a poor ductility, a brittle failure is more likely to occur.

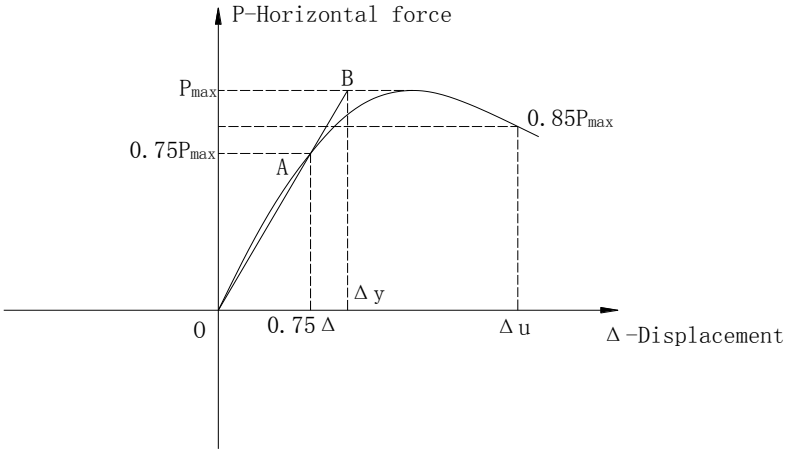

Fig. 11 Definition of the yield and ultimate displacements

Table 4 Loading characteristics and ductility ratios of CFST laced columns

Specimen Number	SCC1	SCC4	SCC5	SCC6
Yield load /*kN*	58.3	52.47	34.11	25.61
Yield displacement Δ_y /*mm*	8.38	8.52	15.94	22.22
Ultimate load/*kN*	79.42	73.77	49.6	33.48
Ultimate displacement Δ_u /*mm*	32.42	30.82	59.61	89.83
Failure load /*kN*	71.84	60.3	45.59	31.11
Failure displacement /*mm*	72.21	73.15	84	140.63
Displacement ductility ratio (μ)	3.87	3.62	3.74	4.04

However, the displacement ductility seems to be less affected by the slenderness ratio or thickness of limbs. As reported in the literature, the connector of structural members is a critical component in terms of displacement ductility. The stronger the connector is, the better the displacement ductility.

3.7 Stiffness degradation

Under constant displacement amplitude, the characteristics of the gradual decrease of structural stiffness with the accumulation of the number of repeated loads is defined as the stiffness degradation. The fundamental cause to the stiffness degradation is the elastoplastic development of material (i.e., steel and concrete) under low cyclic loading and the cumulative damage. There are several models available to predict the residual stiffness. The excellent reviews on the major fatigue models were provided and the models were well to predict the cyclic stiffness degradation (Osorio *et al*. 2013, Ding *et al*. 2017 and Zhou and Attard 2013). The stiffness degradation model is deemed more applicable to the practical design of a composite structure.

In this study, secant (instead of tangent) stiffness, defined as the ratio of peak loading value to peak displacement value under cyclic loading, k_i expressed by Eq. (8), is adopted

$$k_i = \frac{|^{+}_{-}p_i|}{|^{+}_{-}\Delta_i|} \tag{8}$$

where $^{+}_{-}p_i$ is the peak value on the positive-negative loading curve for the i-th loading cycle and $^{+}_{-}\Delta_i$ is the peak value on the positive-negative displacement curve for the i-th loading cycle.

For Specimens SCC1, SCC4, SCC5, and SCC6, the stiffness degradation rates reach the maximum values of 8.38, 8.52, 15.94, and 22.22 mm respectively at the yield, as shown in Fig. 12. The rates decrease gradually until the respective ultimate displacements of 34.42, 30.82, 59.61, and 89.93 mm are attained. Beyond the ultimate displacement point, the stiffness of a specimen tends to become stabilized, indicating that the stiffness degradation

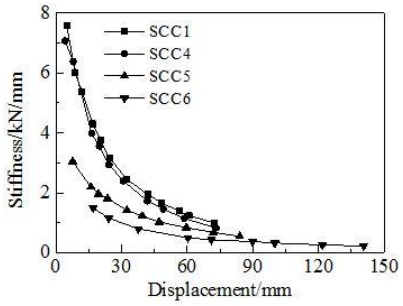

Fig. 12 Stiffness degradation curves

of CFST laced columns is more apparent during the yield stage. The main cause of structural stiffness degradation is the elastoplastic behavior and accumulation of damage under the low cyclic load. Comparing the loading-displacement curves of the test specimens, loading magnitude and cycle number are deemed the important factors affecting the stiffness of the CFST laced columns.

4. Numerical analysis and discussion

4.1 Constitutive model of materials

The accuracy of simulation of column's behavior is strongly determined by the concrete constitutive model used, particularly in terms of the nonlinear behavior, as well as the convergence of numerical analysis. In the plastic damage's study of concrete within ABAQUS, the three widely adopted concrete constitutive models, including smeared cracking model, damaged plasticity model and cracking model of concrete, are used to predict the elastic-plastic and nonlinear behavior of concrete columns under low cyclic loading. The concrete constitutive model in the core area is adopted here with reference to the damaged plasticity model (Yu and Ding 2003). The monotonic concrete stress-strain relation under the compression loading is described by

$$\mathrm{y} = \begin{cases} \dfrac{A_1 x + (B_1 - 1)x^2}{1 + (A_1 - 2)x + B_1 x^2} & x \le 1 \\ \dfrac{x}{\partial_1 (x-1)^2 + x} & x > 1 \end{cases} \tag{9}$$

where $y = \sigma/f_c$, $x = \varepsilon/\varepsilon_c$, $f_c = 0.4 f_{cu}^{\frac{7}{6}}$, $\varepsilon_c = 383 f_{cu}^{\frac{1}{3}} \times 10^{-6}$, $A_1 = 9.1 f_{cu}^{-4/9}$, $B_1 = 1.6(A_1 - 1)^2$,and $\partial_1 = 2.5 f_{cu}^3 \times 10^5$.

According the test results and Eq. (9), the stress-strain relationship of concrete under the compression loading can be established as

$$\sigma = \begin{cases} \dfrac{\varepsilon^2 + 1.22\times10^{-3}\varepsilon}{0.11\varepsilon^2 + 1.44\times10^{-5}\varepsilon + 3.98\times10^{-8}} & \varepsilon \le 1.05\times10^{-3} \\ \dfrac{6.67\times10^{-12}\varepsilon}{\varepsilon^2 - 2.10\times10^{-3}\varepsilon + 1.10\times10^{-6}} & \varepsilon > 1.05\times10^{-3} \end{cases} \tag{10}$$

While the monotonic concrete stress-strain relation

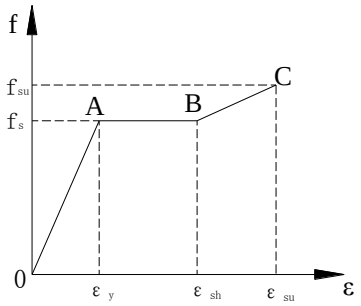

Fig. 13 Stress and strain relationship of steel

under the tension loading is described by

$$y = \begin{cases} \dfrac{A_2 x + (B_2 - 1)x^2}{1 + (A_2 - 2)x + B_1 x^2} & x \le 1 \\ \dfrac{x}{\partial_1 (x-1)^2 + x} & x > 1 \end{cases} \tag{11}$$

where $y = \sigma / f_t$, $x = \varepsilon / \varepsilon_t$, $f_t = 0.24 f_{cu}^{2/3}$, $\varepsilon_t = 33 f_{cu}^{1/3} \times 10^{-6}$, $A_2 = 1.306$, $B_2 = 5\,(A_2 - 1)^2/3 = 0.156$, and $\partial_2 = 1 + 3.4 f_{cu}^2 \times 10^{-4}$.

Eq. (11) results in the following stress-strain relationship of concrete under the tension loading.

$$\sigma = \begin{cases} \dfrac{1.39\times10^{-4}\varepsilon - \varepsilon^2}{2\varepsilon^2 - 4.10\times10^{-5}\varepsilon + 5.34\times10^{-9}} & \varepsilon \le 9.02 \times 10^{-5} \\ \dfrac{\varepsilon}{1.32\times10^{13}\varepsilon^2 - 2.39\times10^{9}\varepsilon + 1.07\times10^{5}} & \varepsilon > 9.02 \times 10^{-5} \end{cases} \tag{12}$$

Compared to the concrete model, the steel models are different from the loading mode and it includes trilinear model, isotropic hardening model, kinematic hardening model and mixed hardening model. In this study, the constitutive model is adopted here with reference to the simply trilinear model. The following Eq. (13) describes the stress-strain relationship.

$$\sigma = \begin{cases} E_s \varepsilon & 0 < \varepsilon \le \varepsilon_y \\ f_s & \varepsilon_y < \varepsilon \le \varepsilon_{sh} \\ f_s + (\varepsilon - \varepsilon_{sh}) E_{st} & \varepsilon > \varepsilon_{sh} \end{cases} \tag{13}$$

where E_s represents the elastic modulus of the steel, $E_{st} = 0.01 E_s$ is the elastic modulus after the steel strengthened. The relationship of the parameters ε_{sh}, f_s, ε_y are shown in Fig. 13.

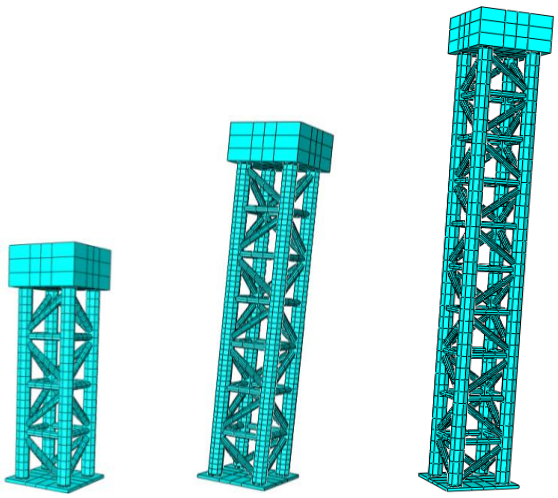

Fig. 14 Representative FE models for CFST laced columns

4.2 Model details and boundary conditions

The FE model was established using ABAQUS program, which was then used extensively to analyze the steel and composite components and structural systems. The accuracy of the FE model has been validated previously (Ding *et al*. 2016). Eight-node brick element (C3D8R) was employed to represent the core concrete in the CFST laced column and the steel plates located at both ends of each specimen. Steel limbs and tubes were represented by the four-node reduced integral format shell elements (S4R).

In order to improve the accuracy and convergence of the analysis, the structured meshing technique was adopted. Selective FE meshes used in the convergence study are shown in Fig. 14. In the normal direction, the interface between the steel and the concrete is defined as a hard contact. In the tangential direction, the coulomb friction model was employed with the friction coefficient of 0.6. Fully coupled binding constraint was imposed between the limb and the tube for ensuring computational efficiency.

The following boundary conditions were assumed in the FE model: Fixed at the bottom of the CFST laced column using ENCASTRE BCs in ABAQUS; Free at the top of the column.

4.3 Comparison between numerical and experimental results

The hysteretic curves of specimens analyzed with their material models were compared with the experimental

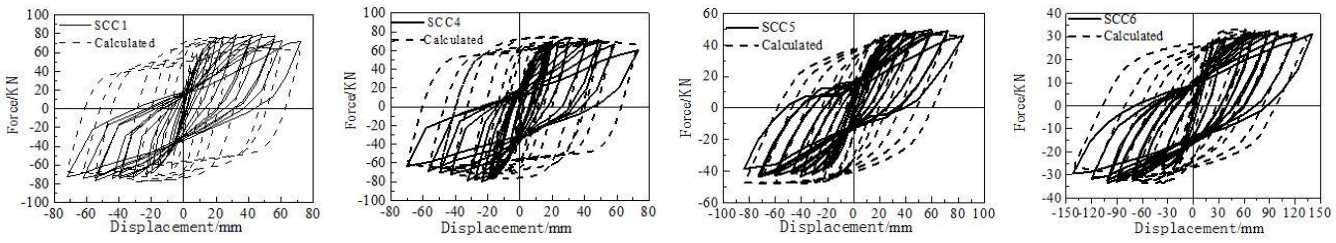

Fig. 15 Comparison of the hysteretic curves for specimens

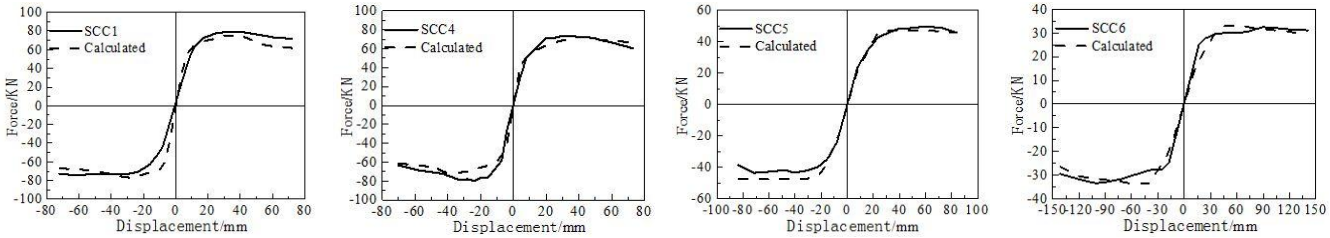

Fig. 16 Comparison of the skeleton curves for specimens

results in Fig. 15. The skeleton curves of the force-displacement relationship were also evaluated (Fig. 16). The experimental results are indicated by a solid line, while the numerical values are displayed by a dashed line.

In most cases, the peaks of the hysteretic curves and the slopes of loading and unloading obtained using the models match the experimental results well. It is worthwhile mentioning that the area enclosed by the hysteretic loop obtained from calculated is stouter than that obtained from experiments, although their shapes are similar (Figs. 15 and 16). This is because some energy dissipation may take place when the concrete cracks open-closed during cyclic loading and unloading. In addition, the bond slip between the steel and the concrete may occur. However, the energy dissipation from the cracks open-closed and the bond slip could not be calculated with ABAQUS. Hence, the pinching phenomenon is observed from experiments.

The comparison shows that the cyclic behavior of the CFST is significantly influenced by the axial compression ratio and the slenderness ratio. Specimens SCC4 with 0.3 axial compression ratio and 10.8 slenderness ratio show a fuller hysteretic loop than that of other specimens. The hysteretic curves of specimens SCC4 SCC6 with 18.4 and 27.9 slenderness ratios respectively become narrow. The analytical hysteretic curves of specimens SCC6 with 0.2 axial compression ratio and 27.9 slenderness ratio is the narrowest. So the axial compression ratio and the slenderness ratio are the most influential factors to the seismic behavior of the CFST laced columns.

4.4 Parameters analysis and discussion

Based on the numerical analysis described in section 4.3, eight specimens with different axial compression ratios between 0.1 and 0.8 were conducted to assess the seismic performance of the CFST laced columns. Thirteen specimens with the column slenderness ratios varying from 4 to 28 were analyzed. To enable an optimal parameter for practical applications of this type of columns in seismic regions, a standard CFST laced column specimen was used with the steel yield strength of 300 MPa and filled with concrete of nominal strength of 40 MPa. The main construction variables of the standard sample are listed in Table 5.

The comparison of the skeleton curves for the specimens with different axial compression ratios is presented in Fig. 17, which indicates that the axial compression ratio (n) has a significant influence on the seismic performance of the CFST laced columns. When n = 0.3, the skeleton curve is more flattened out, signifying a

Table 5 Main construction variables of the standard sample

Length of the column	1500 mm	E_s of steel	206000 MPa
Node distance	300 mm	Strength of tube	300 MPa
Spacing between limbs	300 mm	External diameter of tube	48 mm
External diameter of limb	87 mm	Thickness of tubes	2.0 mm
Thickness of limbs	1.5 mm	Axial compression ratio	0.2

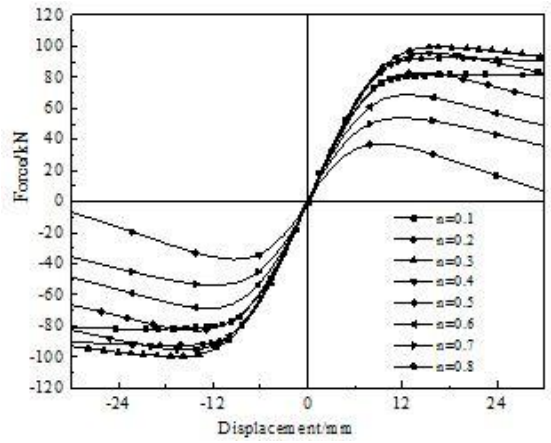

Fig. 17 Comparison of the skeleton curves with different axial compression ratios

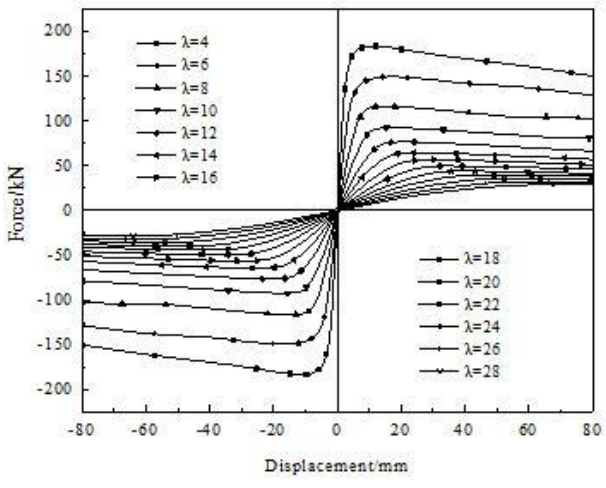

Fig. 18 Comparison of the skeleton curves with different slenderness ratios

better ductility. However, when n > 0.5, the ductility is significantly reduced leading to earlier column failure after the ultimate bearing capacity is reached. Therefore, high axial compression ratios are not recommended for the columns located in seismic regions. According to the study results, it is suggested that the axial compression ratio be kept at 0.2 ~ 0.6 for general CFST laced columns, with n = 0.3 achieving the best.

Due to the complexity of the CFST laced column section and the tedious calculation involved, the nominal slenderness ratio λ, expressed by Eq. (14), is adopted

$$\lambda = \frac{\text{Length of the column (L)}}{\frac{1}{2} \times \text{Spacing between limbs}} \tag{14}$$

The skeleton curves of specimens with different column slenderness ratios are shown in Fig. 18. The figures indicate that λ has a great influence on the skeleton curve of a CFST laced column. In general, with the increasing slenderness ratio, the stiffness in the elastic stage, the yield displacement, and the ultimate displacement increase. While, the maximum horizontal bearing capacity and the stiffness in the descending branch decreased. When λ < 10, the overall cost would be lower. Therefore, it is suggested that λ be kept under 10 when designing a CFST laced column. For longer members, the overall bearing capacity may be improved by increasing the limb spacing.

5. Conclusions

Cyclic tests on six CFST laced columns (consisting of 4 tubes) were conducted to study the failure characteristics, hysteresis curves, skeleton curves, and loading-strain curves. Deformation restoring capacity, displacement ductility, and stiffness degradation are used to analyze the aseismic performance of these specimens. Based on this experimental study, the following observations and conclusions are offered:

(1) The test specimens would fail in compression bending shear and/or compression bending mode under cyclic loading. Overall, the hysteretic loops appear as a full bow-shape. An insignificant pinch phenomenon would appear for long columns due to the uncertain pouring quality of concrete. As a result, the studied CFST laced columns seem to have a good seismic performance.

(2) The bearing capacity and yield displacement of the test specimens increase with the increase of the slenderness ratio. The slenderness ratio of CFST laced columns has a significant influence on the seismic performance. Moreover, with the increasing slenderness ratio the bending failure characteristic is more obvious and the hysteretic loops become stouter. It is suggested that the slenderness ratio be kept at less than 10 for the seismic design of CFST laced columns.

(3) The effect of the axial compression ratio on the hysteresis curves is manifested during the destruction stage. The ultimate bearing capacity values of the test specimens are close to each other when the axial compression ratio is between 0.2 and 0.3, so as the displacement values. In contrast, with a larger axial compression ratio the strength degradation becomes more obvious during the failure stage. The ductility ratio is greater than 3.0 for all test specimens, sufficiently meeting the seismic performance requirements as described in the Chinese design code GB50011-2010. It is suggested that the axial compression ratio of the general CFST laced column be kept at 0.2 ~ 0.6. When the axial compression ratio is around 0.3, the overall seismic performance of the column appears to be best.

(4) Under the low cyclic loading, the stiffness degradation and residual deformation share the same law for CFST laced columns. In the elastic stage, their change is slow, but becomes more apparent in the yield stage. Eventually, the rate of the change of the stiffness degradation and residual deformation ratio will approach to a steady level.

(5) The comparison between numerical and experimental results reveal that the experimental data most accurately. The numerical curves are fuller than that obtained from the experiment. The concrete damaged plasticity model and steel trilinear model are appropriate to predict the nonlinear behavior of CFST laced columns under low cyclic loading.

Acknowledgments

The authors would like to express their gratitude for the financial supports provided by National Natural Science Foundation of China (Grant No. 51378502, 51408449), the Special Fund of Strategic Leader in Central South University (Grant No. 2016CSU001), and China Scholarship Council. The opinions expressed in this paper are solely of the authors, however.

References

Abed, F., Aihamaydeh, M. and Abdalla, S. (2013), "Experimental and numerical investigations of the compressive behavior of concrete filled steel tubes (CFSTs)", *J. Constr. Steel Res.*, **80**, 429-439.

Akihiko, K. and Chiaki, M. (2002), "Cyclic local buckling and fracture of concrete filled tubular members", *Proceedings of the Conference*: *Composite Construction in Steel and Concrete IV*. Banff, Alta., Canada, May.

Choi, K.K., Shin, D.W. and Park, H.G. (2014), "Experimental investigation on structural performance of mega column to spandrel beam connections used in high-rise building", *Struct. Des. Tall Spec.*, **23**(17), 1315-1328.

Ding, F.X., Liu, J., Liu, X.M., and Guo, F.Q. (2016), "Flexural stiffness of steel-concrete composite beam under positive moment", *Steel Compos. Struct., Int. J.*, **20**(6), 1369-1389.

Ding, F.X., Tan, L., Liu, X.M. and Wang, L.P. (2017), "Behavior of circular thin-walled steel tube confined concrete stub columns", *Steel Compos. Struct., Int. J.*, **23**(2), 229-238.

GB50010-2010 (2010a), Code for design of concrete structures;

China Architecture & Building Press, Beijing, China.
GB50010-2010 (2010b), Code for design of concrete structures; China Architecture & Building Press, Beijing, China.
Gong, Y.Z., Zhang, J.W., Jiang, L.Z. and Tu, Y.M. (2010), "Aseismic behavior of concrete columns reinforced with CFRP", *J Central South Univ*., **41**(4), 1506-1514.
Guo, Z.H. (1999), *Principles of Reinforced Concrete*, Tsinghua University Press, Beijing, China.
Han, L.H. and Yao, G.H. (2004), "Experimental behaviour of thin-walled hollow structural steel (HSS) columns filled with self-consolidating concrete (SCC)", *Thin-Wall Struct*., **42**(9), 1537-1377.
Hassanein, M.F., Kharoob, O.F. and Gardner, L. (2015), "Behaviour and design of square concrete-filled double skin tubular columns with inner circular tubes", *Eng. Struct*., **100**, 410-424.
Hedayat, A.S., Sloane, N.A.J. and Stufken, J. (1999), *Orthogonal Arrays*: *Theory and Applications*, Springer, New York, NY, USA.
Jayaganesh, S., Murugadoss, J.R., Prabhu, G.G. and Jegan, J. (2015), "Effects of concentrical partial (local) compression on the structural behavior of concrete filled steel tubular column", *Adv. Mater. Sci. Eng*., 1-9.
Jiang, L.Z., Zhou, W.B. Yu, Z.W. and Zhang, J.J. (2010), "Experimental study and theoretical analysis on the ultimate load carrying capacity of four-tube concrete filled steel tubular lattice columns", *China Civil Eng. J*., **43**(9), 55-62.
Kalochairetis, K.E. and Gantes, C.J. (2011), "Numerical and analytical investigation of collapse loads of laced built-up columns", *Comput. Struct*., **89**(11-12), 1166-1176.
Kawano, A. and Sakino, K. (2003), "Seismic resistance of CFT trusses", *Eng. Struct*., **25**(5), 607-619.
Lachemi, M., Hossain, K.M.A. and Lambros, V.B. (2006), "Self-consolidating concrete filled steel tube columns - Design equations for confinement and axial strength", *Struct. Eng. Mech., Int. J*., **22**(5), 541-562.
Li, G.C., Yang, Z.J., Lang, Y. and Fang, C. (2016), "Behavior of CFST columns with inner CFRP tubeunder biaxial eccentric loading", *Steel Compos. Struct., Int. J*., **22**(6), 1487-1505.
Osorio, E, Bairan, J.M. and Mari, A.R. (2013), "Lateral behavior of concrete under uniaxial compressive cyclic loading", *Mater. Struct*., **46**(5), 709-724.
Ou, Z.J., Chen, B.C., Kai, H.H., Halling, M.W. and Barr, P.J. (2011), "Experimental and analytical investigation of concrete filled steel tubular columns", *ASCE J. Struct. Eng*., **137**(6), 635-645.
Patel, V.I., Liang, Q.Q. and Hadi, M.N.S. (2017), "Nonlinear analysis of circular high strength concrete-filled stainless steel tubular slender beam-columns", *Eng. Struct*., **130**, 1-13.
Portolés, J.M., Romero, M.L., Bonet, J.L. and Filippou, F.C. (2011), "Experimental study of high strength concrete-filled circular tubular columns under eccentric loading", *J. Constr. Steel. Res*., **67**(4), 623-633.
Portolés, J.M., Serra, E. and Romero, M.L. (2013), "Influence of ultra-high strength infill in slender concrete-filled steel tubular columns", *J. Constr. Steel Res*., **86**(7), 107-114.
Xiao, Y.F., Zeng, L. and Cui, Z.K. (2017), "Experimental and analytical performance evaluation of steel beam to concrete-encased composite column with unsymmetrical steel section joints", *Steel Compos. Struct., Int. J*., **23**(1), 17-29.
Yang, M.G., Cai, C.S. and Chen, Y. (2015), "Creep performance of concrete-filled steel tubular (CFST) columns and applications to a CFST arch bridge", *Steel Compos. Struct., Int. J*., **19**(1), 111-129.
Yu, Z.W. and Ding, F.X. (2003), "Unified calculation method of compressive mechanical properties of concrete", *J. Build. Struct*., **24**(4), 41-46.
Zhou, H.Y. and Attard, T.L. (2013), "Rehabilitation and strength sustainability of fatigue damaged concrete-encased steel flexural members using a newly developed polymeric carbon-fiber composite", *Compos. Part. B-Eng*., **45**(1), 1091-1103.

CC